

# Demonstration of a Reconfigurable Entangled Radiofrequency-Photonic Sensor Network

Yi Xia<sup>#,1</sup>, Wei Li<sup>#,2,\*</sup>, William Clark,<sup>3</sup> Darlene Hart,<sup>4</sup> Quntao Zhuang,<sup>5,1</sup> and Zheshen Zhang<sup>2,1,†</sup>

<sup>1</sup>James C. Wyant College of Optical Sciences, University of Arizona, Tucson, Arizona 85721, USA

<sup>2</sup>Department of Materials Science and Engineering,  
University of Arizona, Tucson, Arizona 85721, USA

<sup>3</sup>General Dynamics Mission Systems, 8220 East Roosevelt Street, Scottsdale, Arizona 85257, USA

<sup>4</sup>General Dynamics Mission Systems, 9 Vreeland Road, Florham Park, New Jersey 07932, USA

<sup>5</sup>Department of Electrical and Computer Engineering,  
University of Arizona, Tucson, Arizona 85721, USA

Quantum metrology takes advantage of nonclassical resources such as entanglement to achieve a sensitivity level below the standard quantum limit. To date, almost all quantum-metrology demonstrations are restricted to improving the measurement performance at a single sensor, but a plethora of applications require multiple sensors that work jointly to tackle distributed sensing problems. Here, we propose and experimentally demonstrate a reconfigurable sensor network empowered by continuous-variable (CV) multipartite entanglement. Our experiment establishes a connection between the entanglement structure and the achievable quantum advantage in different distributed sensing problems. The demonstrated entangled sensor network is composed of three sensor nodes each equipped with an electro-optic transducer for the detection of radiofrequency (RF) signals. By properly tailoring the CV multipartite entangled states, the entangled sensor network can be reconfigured to maximize the quantum advantage in distributed RF sensing problems such as measuring the angle of arrival of an RF field. The rich physics of CV multipartite entanglement unveiled by our work would open a new avenue for distributed quantum sensing and would lead to applications in ultrasensitive positioning, navigation, and timing.

Quantum metrology [1–4] enables a measurement sensitivity below the standard quantum limit (SQL), as demonstrated in the Laser Interferometer Gravitational-wave Observatory (LIGO) [5–8]. As a unique quantum resource, entanglement has been utilized to enhance the performance of, e.g., microscopy [9], target detection [10], and phase estimation [11]. To date, almost all existing entanglement-enhanced sensing demonstrations operate at a single sensor by entangling the probe with a local reference, but a multitude of applications rely on an array of sensors that work collectively to undertake sensing tasks. On the other hand, entanglement-enhanced optical sensing has been extensively explored, while many useful sensing applications for, e.g., positioning and astronomy operate in the radiofrequency (RF) and microwave spectral ranges. In this regard, quantum illumination enables a signal-to-noise ratio (SNR) advantage over classical schemes in the RF and microwave where ambient noise is abundant [10, 12–16], but quantum illumination has a limited operational range and quantum enhancement [10, 15, 16], due to large diffraction in the microwave and a lack of efficient quantum memories.

Recent theoretical advances in distributed quantum sensing (DQS) promise a boosted performance for distributed sensing problems. Compared with DQS based on discrete-variable (DV) multipartite entanglement [17, 18], continuous-variable (CV) DQS [19, 20] enjoys deterministic preparation of multipartite entangled probe

states and robustness against loss. Fig. 1a illustrates CV-DQS: A squeezed vacuum state with a mean photon number  $N_S$  is processed by a quantum circuit consisting of beam splitters (BSs) and phase shifters to create a CV multipartite entangled state in  $M$  modes,  $\{\hat{b}^{(m)}, 1 \leq m \leq M\}$ , shared by  $M$  sensors. The sensing attempt is modeled by a quadrature displacement operation  $\hat{D}(\alpha_m)$  on each mode. The distributed sensing problem is to estimate a global property across all sensors. Let the probed global parameter be  $\bar{\alpha} \equiv \sum_{m=1}^M v_m \alpha_m$ , where the weights,  $\{v_m, 1 \leq m \leq M\}$ , define the global parameter estimation problem. To estimate the displacements, homodyne measurements yield outcomes  $\tilde{\alpha}_m$ 's, followed by classical postprocessing that obtains an estimation  $\tilde{\alpha} = \sum_m v_m \tilde{\alpha}_m$ .

Critically, the quantum circuit must be optimized to generate a CV multipartite entangled state that minimizes the estimation variance in a given distributed sensing problem. Since  $\tilde{\alpha}$  is obtained as if an effective mode  $\sum v_m \hat{b}^{(m)}$  is homodyned, the minimum estimation variance is attained when the effective mode equals the original squeezed vacuum mode  $\hat{b}$ . As such, the optimum quantum circuit distributes  $v_m$  amplitude portion of the squeezed vacuum state to the  $m$ -th sensor, leading to the minimum estimation variance:

$$\delta\alpha^2 = \frac{\bar{v}^2}{4} \left[ \frac{\eta}{(\sqrt{N_S + 1} + \sqrt{N_S})^2} + 1 - \eta \right], \quad (1)$$

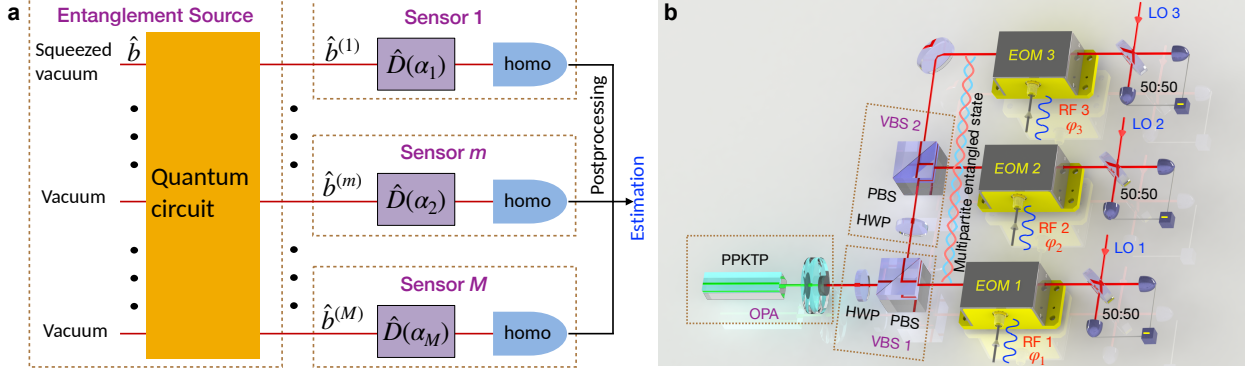


FIG. 1. (a) The CV-DQS protocol. A squeezed-vacuum mode  $\hat{b}$  is processed by a quantum circuit to produce a multipartite entangled state between  $\hat{b}^{(m)}$ 's. The sensing process is modeled by displacement operations  $\hat{D}(\alpha_m)$ 's followed by homodyne measurements (homo), whose outcomes are postprocessed to produce an estimation. (b) Experimental diagram. Phase squeezed light is generated from a periodically-poled KTiOPO<sub>4</sub> (PPKTP) crystal embedded in an optical parametric amplifier (OPA) cavity. A quantum circuit comprising two variable BSs (VBSs) configures the CV multipartite entangled state for different distributed sensing tasks. Each VBS consists of a half-wave plate (HWP) and a polarizing BS (PBS). An RF-photonic sensor entails an electro-optic modulator (EOM) and a balanced homodyne detector supplied by a local oscillator (LO) interfering the signal on a 50:50 BS.  $\varphi_m$ : RF phase.

where  $\bar{v} \equiv \sqrt{\sum_{m=1}^M v_m^2}$ , and  $1 - \eta$  is the loss at the each sensor.

Ref. [31] derived an upper bound for the Fisher information by explicitly reducing it to quadrature variances. The CV-DQS protocol saturates the upper bound in the absence of loss, i.e.,  $\eta = 1$ , and is therefore the optimum among *all* protocols subject to a photon-number constraint for the probe. Specifically, at  $\eta = 1$  and a fixed mean photon number  $n_s \equiv N_S/M$  at each sensor, equal weights yield  $\delta\alpha^2 \propto (1/M)^2 \times 1/n_s$ , i.e., a Heisenberg scaling for the estimation variance with respect to the number of sensors, whereas any protocol without entanglement is subject to the SQL. Also,  $M = 1$  and  $\bar{v} = 1$  reduce the situation to single parameter estimation enhanced by a single-mode squeezed vacuum state. In the presence of loss, the Fisher-information upper bound becomes loose. However, by reducing the multi-parameter estimation problem to a single-parameter estimation problem through a fictitious set of conjugating beamsplitters, it was shown that the CV-DQS protocol remains the optimum among all protocols based on Gaussian states or homodyne measurements [19]. Importantly, the entanglement-enabled advantage in the CV-DQS protocol survives arbitrary amount of loss, even though loss precludes a Heisenberg scaling.

On the experimental front, a recent work [21] showed that CV entanglement offers a measurement-sensitivity advantage in optical phase estimation over using separable states, but the connection between the entanglement structure and the enabled quantum advantage in

different distributed sensing problems have not been experimentally explored. Moreover, the CV-DQS protocol [19] represents a general framework for tackling sensing problems in different physical domains, because quantum transducers can convert the probed physical parameter to quadrature displacement. Here, we demonstrate a reconfigurable entangled sensor network equipped with electro-optic transducers (EOTs) for entanglement-enhanced measurements of RF signals. Our experiment unveils how the CV multipartite entanglement structure determines the quantum advantage in different distributed sensing problems. Specifically, by tailoring the entanglement shared by the sensors, the entangled RF-photonic sensor network achieves an estimation variance 3.2 dB below the SQL in measuring the average RF field amplitudes. Also, in measuring the angle of arrival (AoA) of an emulated incident RF wave, the entangled RF-photonic sensor network achieves an estimation variance 3.2 dB below the SQL via phase-difference estimation at an edge node and 3.5 dB below the SQL via phase-difference estimation at a central node.

The experiment is illustrated in Fig. 1b. Sideband phase squeezed state is generated from an optical parametric amplifier (OPA) and subsequently processed by a quantum circuit comprised of two variable BSs (VBSs) to produce a CV multipartite entangled state shared by three RF-photonic sensors. The RF field at the  $m$ -th sensor is represented by  $\mathcal{E}_m(t) = E_m \cos(\omega_c t + \varphi_m)$ , where  $\omega_c$  is the carrier frequency,  $E_m$  is the amplitude, and  $\varphi_m$

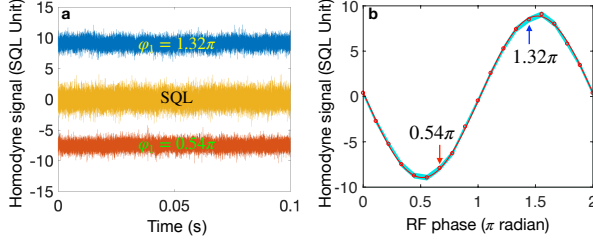


FIG. 2. (a) Time-domain traces of the homodyne output signals at  $\varphi_1 = 0.54\pi$  (red) and  $1.32\pi$  (blue), showing a 4-dB noise reduction as compared with the SQL (gold). The shot-noise limit of the homodyne measurements dictates the SQL and is normalized to a standard deviation of 1. (b) The homodyne output signals at different RF phases. All signals are normalized using the same factor for the SQL normalization. Circles: the means of the measured homodyne signals; red curve: a sinusoidal fit; shaded area: normalized standard deviation of the measurement noise.

is the phase of the RF field. At each sensor, an electro-optic modulator (EOM) driven by the probed RF field induces a displacement on the squeezed phase quadrature, as described by

$$\alpha_m \simeq i\sqrt{2}\pi g_m a_c^{(m)} \frac{\gamma E_m}{2V_\pi} \varphi_m, \quad (2)$$

where  $g_m = \pm 1$  is set by an RF signal delay that controls the sign of the displacement,  $a_c^{(m)}$  is the amplitude of the baseband coherent state at the  $m$ -th sensor,  $V_\pi$  is the half-wave voltage of the EOM, and  $\gamma$  models the conversion from an external electric field to the internal voltage (see Ref. [22]’s Sec. I A). To estimate the displacement, a local oscillator (LO) interferes the signal on a 50:50 BS for a balanced homodyne measurement. The time-domain data from the three homodyne measurements are postprocessed to derive the estimated parameter and the associated estimation variance under different settings.

Prior to constructing an entangled sensor network, we first assess RF-photon sensing enhanced by single-mode squeezed light. To do so, VBS 1 is configured to deliver all light to Sensor 1. Fig. 2a first plots in the gold curve a calibrated shot-noise level with standard deviation normalized to 1 to represent the SQL. The blue and red curves are, respectively, the traces at  $\varphi_1 = 0.54\pi$  and  $1.32\pi$  and are normalized using the same factor as that for the gold curve. The variances of the curves reflect the quantum measurement noise, which in turn determines the estimation variance. Beating the SQL is a nonclassical characteristic, as witnessed in the variances of the red and blue curves. Both cases suppress the SQL by  $\sim 4$  dB. The means of the time-domain homodyne traces, as

the phase of the RF field is swept, are then scaled to the SQL unit and plotted as red circles in Fig. 2b, showing a nice fit to a sinusoidal function, as expected.

We now demonstrate the power of CV multipartite entanglement in three distributed RF sensing tasks. First, the average RF-field amplitude at the three sensors is estimated using an equally weighted CV multipartite entangled state, which yields the optimum performance (see Ref. [22]’s Sec. I). The RF-field amplitude at Sensor 1 is swept from 20 mV to 160 mV while keep the amplitudes of Sensor 2 and 3 at 80 mV. The homodyne data from the three sensors are first averaged and then scaled to ensure an unbiased estimator. The estimates are plotted as blue circles in Fig. 3a, with the blue shaded area representing the estimation uncertainty due to quantum measurement noise. The deviation from the linear fit is caused by instability in phase locking. As a comparison, the estimated average RF-field amplitudes by a classical separable sensor network are plotted as red triangles in the same figure, with the red shaded area representing the estimation uncertainty. The entangled sensor network shows a reduced estimation variance of 3.2 dB.

We then estimate the AoA of an emulated incident RF field. In a one-dimensional sensor array, this sensing problem is translated into the estimation of the phase difference across the sensors, which can be solved by a finite difference method [22]. To estimate the phase difference at an edge node (served by Sensor 2 in the experiment), the optimum weights for the CV multipartite entangled state are  $[-3/2, 2, -1/2]$ , generated by setting the splitting ratios (reflectivity:transmissivity) of the VBSs to 50:50 and 75:25. The negative signs in the weights are introduced by adding  $\pi$ -phase delays at Sensor 2 and Sensor 3. In this measurement, the RF phase at Sensor 1 and 3 is swept from  $-0.17$  rad to  $0.17$  rad while the RF phase at Sensor 2 is set to 0. The estimated phase difference vs. the applied RF-field phase are plotted in Fig. 3b for the entangled scheme (blue circles) and compared to that of the classical separable scheme (red triangles) networks with the shaded area representing the estimation uncertainties, showing a 3.2-dB reduction in the estimation variance for the entangled case.

While quantum noise arises in each homodyne measurement, a proper multipartite entangled state leads to a reduction in the overall estimation variance, whereas such a noise reduction mechanism is absent in a classical separable sensor network. Figure 3c and d show such a behavior. The measurement noise variances at the three sensors, represented by green, gold, and magenta, are plotted for both the entangled (circles) and classical separable (triangles) cases in the SQL unit. To facilitate the

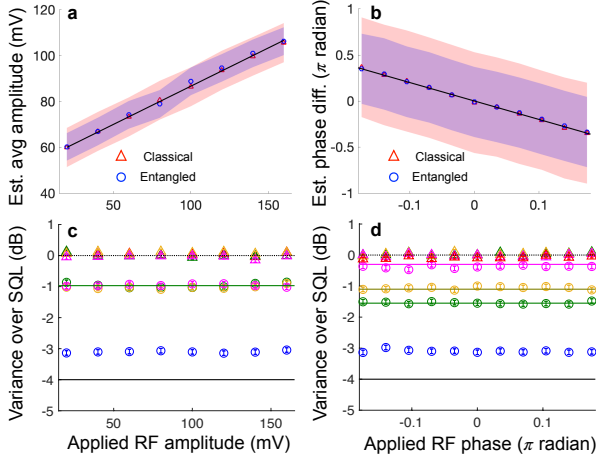


FIG. 3. Estimation of (a) average field amplitude and (b) phase difference at an edge node. Circles: data for entangled sensors; triangles: data for classical separable sensors. Shaded area: estimation uncertainties for the entangled (blue) and classical separable (red) sensor networks. The entangled sensors show a clear reduced estimation uncertainty. Noise variances at (c) different field amplitudes and (d) at different phase differences at an edge node. In (c) and (d), measurement noise variances are plotted in green for Sensor 1, gold for Sensor 2, and magenta for Sensor 3. Estimation variances, normalized to the SQL, for entangled (blue) and classical separable (red) sensor networks. Green, gold, and magenta solid horizontal lines: theory curves for noise variances at three sensors. Solid black horizontal line: ideal estimation variance for entangled sensors; experimental deviation likely caused by imperfect phase locking between sensors. Dotted black horizontal line: the SQL for measurement noise variances and normalized estimation variances. While all classical data stay at the SQL, the estimation variances for the entangled sensor networks are sub-SQL and are significantly lower than the measurement noise variances at single sensors. Error bars reflect estimated measurement uncertainties caused by system instabilities.

comparison, the estimation variances for the three tasks are also normalized to the SQL using a factor predetermined by the weights and are depicted as blue circles and red triangles for, respectively, the entangled and classical separable cases. It is evident that all classical data stay at the SQL. For the entangled sensor network, while the noise variances at each sensor barely suppresses the SQL by  $\sim 1$  dB, the normalized estimation variances, however, substantially beats the SQL by  $3.2 \pm 0.1$  dB.

A unique aspect of an entangled sensor network is that a proper multipartite entangled state need be prepared to achieve the optimum performance in a specific distributed sensing task. To show this, the splitting ratio for VBS 2 is varied to prepare different entangled states for the task of RF-field phase-difference estimation at an

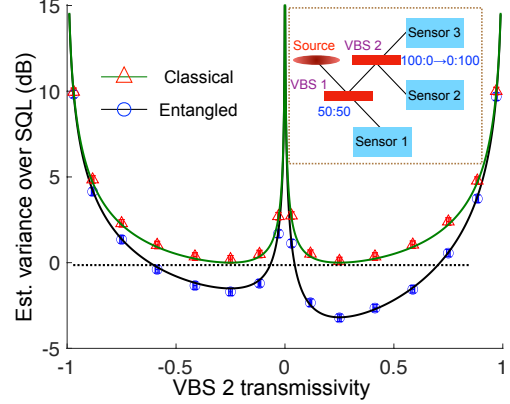


FIG. 4. Optimization of CV multipartite entangled state for phase difference at an edge node. Circles: data for entangled sensors; triangles: data for classical separable sensors; black curves: quantum theory; green curves: classical theory. Black horizontal dotted line: the SQL. Error bars account for estimated uncertainties arising from experimental instabilities. The symmetric classical curves vs. the asymmetric quantum curves manifest the correlated quantum noise arising from the homodyne detectors at different sensors. Inset: illustration of the tuning ranges of the splitting ratios for VBSs.

edge node (see inset of Fig. 4). The resulting estimation variances are compared with these for the classical separable sensor network under the same VBS settings. In the measurements, a positive transmissivity means the sign of homodyne data remains unchanged in postprocessing while a  $\pi$ -phase delay is introduced to the RF signal. This is equivalent to applying a  $\pi$ -phase shift on the quantum state at Sensor 3, followed by a sign flip on its homodyne data. A negative transmissivity indicates a sign flip is applied to Sensor 3's homodyne data in postprocessing and no  $\pi$ -phase delay on the RF signal. An unbiased estimator is ensured in either case.

The estimation variance vs. transmissivity curves show very different behaviors for the entangled and classical separable cases. The curves for the classical separable case are symmetric, with the minimum estimation variances found at both positive and negative transmissivities, whereas the curves for the entangled case display a strong asymmetric characteristic. Such a behavior manifests the quantum correlation shared by the sensors. In a classical separable sensor network, the quantum measurement noise is independent at different sensors, so postprocessing on the measurement data to acquire an unbiased estimator does not alter the noise power. In an entangled sensor network, however, the quantum measurement noise at different sensors is correlated, so it can only be reduced to minimum if the ho-

modyne data from different sensors are added up with a proper set of weights. Importantly, these weights also need to ensure an unbiased estimator. As such, tailoring a proper CV multipartite entangled state for a specific distributed sensing problem to simultaneously satisfy the two criteria is critical to achieve a large quantum advantage over a classical separable sensor network.

Before closing, a few remarks are worth making. First, our experiment opens a window for quantum-enhanced RF-photonic sensing [23], which outperforms electronics-based sensing in its large processing bandwidths, engineered RF responses using optical filters, and capability of transporting RF signals over long distances via optical fibers [24]. A recent photonics-based coherent radar system demonstrated key performance metrics such as a signal-to-noise ratio of  $73 \text{ dB MHz}^{-1}$  and a spurious-free dynamic range of  $70 \text{ dBc}$ , comparable with state-of-the-art electronics-based radar systems'  $80 \text{ dB MHz}^{-1}$  and  $70 \text{ dBc}$  [25]. Higher RF-to-photonic conversion efficiency, determined by the  $V_\pi$  of the EOT, can further increase the measurement sensitivity. State-of-the-art EOTs based on, e.g., piezoptomechanical coupling [26], ultrasmall cavities [27], organic EO-plasmonic nanostructures [28], and highly nonlinear ferroelectric materials [29], can achieve  $V_\pi < 0.1 \text{ V}$  [26] and thus increase the measurement sensitivity by  $> 60 \text{ dB}$ . It is worth noting that the quantum advantage survives low RF-photonic conversion efficiency, assuming the same EOTs are employed in both the entangled and classical separable sensor networks. Second, in our experiment, the anti-squeezing level at the source is  $\sim 10 \text{ dB}$  and the squeezing level is  $\sim 4 \text{ dB}$ , from which we can infer the ideal source squeezing of  $\sim 11.7 \text{ dB}$  ( $N_S \sim 3.3$ ). The measured squeezing was  $\sim 3.2 \text{ dB}$  for the sensor network. Thus, an overall efficiency  $\eta \sim 0.56$  is derived. With equal weights, the optimum separable scheme employs  $\sim 7.9 \text{ dB}$  of local squeezing at each sensor [19] to match the total mean photon number and achieves a  $2.7 \text{ dB}$  of noise reduction. This leads to a  $\sim 10\%$  advantage in estimation variance for our experimental result over that of the optimum separable sensor network, thereby verifying the entanglement shared by the sensors [30]. Third, while the current entangled RF-photonic sensor network cannot beat the ultimate estimation precision limit set by the RF sky temperature, it does offer an advantage over a classical RF-photonic sensor network under the same task, assuming sensors are connected by low-loss optical fibers that distribute entanglement over a few kilometers without significant loss penalty [22]. To further enlarge the operational range, noiseless linear amplifiers [31, 32] or CV error correction [33, 34] can be

used to overcome loss. Fourth, the entangled sensor network does not require quantum memories, but with the assistance of quantum memories it will be able to extract time-domain information more effectively.

In conclusion, we implemented a reconfigurable entangled RF-photonic sensor network and demonstrated sub-SQL estimation variances in distributed sensing tasks. A connection between the entanglement structure and nonclassical quantum noise reduction was established. This quantum-sensing paradigm would create opportunities for ultrasensitive position, navigation, timing, astronomy, and imaging applications.

We thank Jeffrey Shapiro and Franco Wong for their valuable feedback on the manuscript and Saikat Guha for helpful discussions. We also thank an anonymous Referee's comments, which have helped us significantly improve the manuscript. This work is funded by General Dynamics Mission Systems and the Office of Naval Research Award No. N00014-19-1-2190. We also thank the University of Arizona for the support in the quantum research.

---

\* Current address: Department of Electronic and Information Engineering, Shanxi University, Taiyuan, China

† zsz@email.arizona.edu

# Equal contributions

- [1] S. Pirandola, B. R. Bardhan, T. Gehring, C. Weedbrook, and S. Lloyd, Advances in photonic quantum sensing, *Nat. Photon.* **12**, 724–733 (2018).
- [2] C. L. Degen, F. Reinhard, and P. Cappellaro, Quantum sensing, *Rev. Mod. Phys.* **89**, 035002 (2017).
- [3] V. Giovannetti, S. Lloyd, and L. Maccone, Advances in quantum metrology, *Nat. Photon.* **5**, 222 (2011).
- [4] S. H. Tan, and P. P. Rohde, The resurgence of the linear optics quantum interferometer—recent advances & applications, *Rev. Phys.* **4**, 100030 (2019).
- [5] J. Abadie *et al.* (LIGO Collaboration), A gravitational wave observatory operating beyond the quantum shot-noise limit, *Nat. Phys.* **7**, 962–965 (2011).
- [6] J. Aasi *et al.* (LIGO Collaboration), Enhanced sensitivity of the LIGO gravitational wave detector by using squeezed states of light, *Nat. Photon.* **7**, 613–619 (2013).
- [7] M. Tse *et al.* (LIGO Collaboration), Quantum-Enhanced Advanced LIGO Detectors in the Era of Gravitational-Wave Astronomy, *Phys. Rev. Lett.* **123**, 231107 (2019).
- [8] F. Acernese *et al.* (Virgo Collaboration), Increasing the Astrophysical Reach of the Advanced Virgo Detector via the Application of Squeezed Vacuum States of Light, *Phys. Rev. Lett.* **123**, 231108 (2019).
- [9] T. Ono, R. Okamoto, and S. Takeuchi, An entanglement-enhanced microscope, *Nat. Commun.* **4**, 2426 (2013).
- [10] Z. Zhang, S. Mouradian, F. N. C. Wong, and J. H. Shapiro,

- Entanglement-enhanced sensing in a lossy and noisy environment, *Phys. Rev. Lett.* **114**, 110506 (2015).
- [11] G. Colangelo, F. Martin Ciurana, G. Puentes, M. W. Mitchell, and R. J. Sewell, Entanglement-enhanced phase estimation without prior phase information, *Phys. Rev. Lett.* **118**, 233603 (2017).
- [12] S.-H. Tan, B. I. Erkmen, V. Giovannetti, S. Guha, S. Lloyd, L. Maccone, S. Pirandola, and J. H. Shapiro, Quantum illumination with Gaussian states, *Phys. Rev. Lett.* **101**, 253601 (2008).
- [13] E. D. Lopaeva, I. Ruo Berchera, I. P. Degiovanni, S. Olivares, G. Brida, and M. Genovese, Experimental realization of quantum illumination, *Phys. Rev. Lett.* **110**, 153603 (2013).
- [14] Q. Zhuang, Z. Zhang and J. H. Shapiro, Optimum mixed-state discrimination for noisy entanglement-enhanced sensing, *Phys. Rev. Lett.* **118**, 040801 (2017).
- [15] S. Barzanjeh, S. Guha, C. Weedbrook, D. Vitali, J. H. Shapiro, and S. Pirandola, Microwave quantum illumination, *Phys. Rev. Lett.* **114**, 080503 (2015).
- [16] S. Barzanjeh, S. Pirandola, D. Vitali, and J. M. Fink, Experimental microwave quantum illumination, arXiv:1908.03058.
- [17] T. J. Proctor, P. A. Knott, and J. A. Dunningham, Multiparameter estimation in networked quantum sensors, *Phys. Rev. Lett.* **120**, 080501 (2018).
- [18] W. Ge, K. Jacobs, Z. Eldredge, A. V. Gorshkov, and M. Foss-Feig, Distributed quantum metrology with linear networks and separable inputs, *Phys. Rev. Lett.* **121**, 043604 (2018).
- [19] Q. Zhuang, Z. Zhang, and J. H. Shapiro, Distributed quantum sensing using continuous-variable multipartite entanglement, *Phys. Rev. A* **97**, 032329 (2018).
- [20] Q. Zhuang and Z. Zhang, Physical-layer supervised learning assisted by an entangled sensor network, *Phys. Rev. X* **9**, 041023 (2019).
- [21] X. Guo *et al.*, Distributed quantum sensing in a continuous variable entangled network, *Nat. Phys.* **16**, 281–284(2020).
- [22] See Supplemental Material for details of the theoretical framework, the experimental setup, and additional experimental data. Supplemental Material includes Refs. [35–37].
- [23] D. Marpaung, J. Yao, and J. Capmany, Integrated microwave photonics, *Nat. Photon.* **13**, 80–90 (2019).
- [24] C. Lim *et al.*, Fiber-wireless networks and subsystem technologies, *J. Lightw. Technol.* **28**, 390–405 (2010).
- [25] P. Ghelfi *et al.*, A fully photonics-based coherent radar system, *Nature* **507**, 341–345 (2014).
- [26] W. Jiang *et al.*, Efficient bidirectional piezoptomechanical transduction between microwave and optical frequency, arXiv:1909.04627.
- [27] H. Choi, M. Heuck, and D. Englund, Self-Similar Nanocavity Design with Ultrasmall Mode Volume for Single-Photon Nonlinearities, *Phys. Rev. Lett.* **118**, 223605 (2017).
- [28] W. Heni *et al.*, Plasmonic IQ modulators with attojoule per bit electrical energy consumption, *Nat. Commun.* **10**, 1694 (2019).
- [29] S. Abel *et al.*, Large Pockels effect in micro- and nanostructured barium titanate integrated on silicon, *Nat. Mat.* **18**, 42–47(2019).
- [30] Z. Qin, M. Gessner, Z. Ren, X. Deng, D. Han, W. Li, X. Su, A. Smerzi, and K. Peng, Characterizing the multipartite continuous-variable entanglement structure from squeezing coefficients and the Fisher information, *npj Quantum Inf.* **5**, 3 (2019).
- [31] Y. Xia, Q. Zhuang, W. Clark, and Z. Zhang, Repeater-enhanced distributed quantum sensing based on continuous-variable multipartite entanglement, *Phys. Rev. A* **99**, 012328 (2019).
- [32] T. C. Ralph and A. P. Lund, Nondeterministic noiseless linear amplification of quantum systems, in *Proceedings of the Ninth International Conference on Quantum Communication, Measurement and Computing*, Calgary, 2008, edited by A. Lvovsky, AIP Conf. Proc. No. 1110 (AIP, Melville, 2009), p. 155.
- [33] K. Noh, S. M. Girvin, and L. Jiang, Encoding an oscillator into many oscillators, arXiv:1903.12615.
- [34] Q. Zhuang, J. Preskill, and L. Jiang, Distributed quantum sensing enhanced by continuous-variable error correction, *New J. Phys.* **22**, 022001 (2020).
- [35] M. Mehmet, S. Ast, T. Eberle, S. Steinlechner, H. Vahlbruch, and R. Schnabel, Squeezed light at 1550 nm with a quantum noise reduction of 12.3 dB, *Opt. Express* **19**, 25763 (2011).
- [36] K. Qian, Z. Eldredge, W. Ge, G. Pagano, C. Monroe, J. V. Porto, and A. V. Gorshkov, Heisenberg-scaling measurement protocol for analytic functions with quantum sensor networks, *Phys. Rev. A* **100**, 042304 (2019).
- [37] Y. Tamura, H. Sakuma, K. Morita, M. Suzuki, Y. Yamamoto, K. Shimada, Y. Honma, K. Sohma, T. Fujii, and T. Hasegawa, The First 0.14-dB/km Loss Optical Fiber and its Impact on Submarine Transmission, *J. Light. Technol.* **36**, 44–49 (2018).

# Supplemental Material

## Demonstration of a Reconfigurable Entangled Radiofrequency-Photonic Sensor Network

Yi Xia<sup>#,1</sup>, Wei Li<sup>#,2,\*</sup>, William Clark,<sup>3</sup> Darlene Hart,<sup>4</sup> Quntao Zhuang,<sup>5,1</sup> and Zheshen Zhang<sup>2,1,†</sup>

<sup>1</sup>James C. Wyant College of Optical Sciences, University of Arizona, Tucson, Arizona 85721, USA

<sup>2</sup>Department of Materials Science and Engineering,  
University of Arizona, Tucson, Arizona 85721, USA

<sup>3</sup>General Dynamics Mission Systems, 8220 East Roosevelt Street, Scottsdale, Arizona 85257, USA

<sup>4</sup>General Dynamics Mission Systems, 9 Vreeland Road, Florham Park, New Jersey 07932, USA

<sup>5</sup>Department of Electrical and Computer Engineering,  
University of Arizona, Tucson, Arizona 85721, USA

### I. THEORETICAL FRAMEWORK

We present a detailed theoretical framework for performance analysis. In Section IA, we analyze the single sensor performance and explain the transformation of RF signals into optical displacements. In Section IB, we analyze the performance of a network of sensors with shared continuous-variable (CV) multipartite entanglement and solve the optimum entanglement configuration. In Section IC, we explain an alternative resource counting method and compare the entangled scheme with the optimal separable scheme subject to the photon-number constraint. In Section ID, we connect the measurement results to the parameters of a RF field.

#### A. Single RF-photonic sensor enhanced by squeezed light

We consider an entangled RF-photonic sensor network composed of  $M$  sensors. The quantum states of interest at each sensor are carried on three optical spectral modes, i.e., a central mode  $\hat{a}_c^{(m)}$  at the optical carrier frequency  $\Omega$  and two sideband modes  $\hat{a}_\pm^{(m)}$  at optical frequencies  $\Omega \pm \omega_c$ . Here,  $1 \leq m \leq M$  indexes the sensors. Suppose the probed RF field at the  $m$ -th sensor is represented by the waveform  $\mathcal{E}_m(t) = E_m \cos(\omega_c t + \varphi_m)$ , where  $\omega_c$  is the carrier frequency of the RF field,  $E_m$  is the RF-field amplitude, and  $\varphi_m$  is the RF-field phase. The EOM transduces the RF field into a phase modulation on the optical field so that the spectral mode  $\hat{a}_\omega e^{-i\omega t}$  at  $\omega$  becomes

$$\hat{a}_\omega e^{-i\omega t} e^{i\zeta E_m \cos(\omega_c t + \varphi_m)} = \hat{a}_\omega \sum_{n=-\infty}^{\infty} i^n J_n(A_m) e^{i(-\omega - n\omega_c)t + n\varphi_m}, \quad (\text{S1})$$

where the Jacobi-Anger expansion has been employed,  $J_n(z)$  is the  $n$ -th Bessel function of the first kind. Here  $A_m = \zeta E_m$ , where  $\zeta = \pi\gamma/V_\pi$  accounts for the RF-to-photonic conversion efficiency and the conversion from an external electric field to the applied voltage on the EOM by an antenna as modeled by  $\gamma$ . Effectively, the spectral mode  $\hat{a}_\omega$  undergoes a frequency-domain beam splitter transform and is spread over to the spectral modes  $\omega - n\omega_c$ ,  $n = 0, \pm 1, \pm 2, \dots$ . For small  $A_m$ ,  $J(A_m) \sim (A_m)^n 2^{-n}/n!$  decays quickly with  $n$ . In a weak RF-field scenario, only the  $n = 0, \pm 1$  components need be considered such that  $\hat{a}^{(m)}$ 's undergo an effective frequency-domain beam splitter transform, yielding the transformed spectral mode operators

$$\begin{aligned} \hat{a}_c^{(m)'} &= J_0(A_m)\hat{a}_c^{(m)} + iJ_1(A_m)\hat{a}_-^{(m)} e^{i\varphi_m} + iJ_1(A_m)\hat{a}_+^{(m)} e^{-i\varphi_m} \\ \hat{a}_+^{(m)'} &= J_0(A_m)\hat{a}_+^{(m)} + iJ_1(A_m)\hat{a}_c^{(m)} e^{i\varphi_m} + iJ_1(A_m)\hat{a}_-^{(m)} e^{-i\varphi_m} \\ \hat{a}_-^{(m)'} &= J_0(A_m)\hat{a}_-^{(m)} + iJ_1(A_m)\hat{a}_c^{(m)} e^{i\varphi_m} + iJ_1(A_m)\hat{a}_+^{(m)} e^{-i\varphi_m}, \end{aligned} \quad (\text{S2})$$

where  $\hat{a}_{2\pm}^{(m)}$  are higher-order spectral modes at frequencies  $\Omega \pm 2\omega_c$ , and  $J_{-n}(z) = (-1)^n J_n(z)$  has been used. Initially, all the sideband modes  $\hat{a}_\pm^{(m)}, \hat{a}_{2\pm}^{(m)}$  are in zero-mean states, while the central spectral mode  $\hat{a}_c^{(m)}$  is in a quantum state close to the coherent state  $|\alpha_m\rangle$ . Thus,  $\langle \hat{a}_\pm^{(m)'} \rangle = iJ_1(A_m)e^{\pm i\varphi_m} \alpha_m$ .

The optical field operator carrying the three spectral modes at sensor  $m$  now reads

$$\hat{E}^{(m)}(t) = \hat{a}_c^{(m)'} e^{-i\Omega t} + \hat{a}_+^{(m)'} e^{-i(\Omega + \omega_c)t} + \hat{a}_-^{(m)'} e^{-i(\Omega - \omega_c)t}. \quad (\text{S3})$$

Let the LO optical field be  $E_{\text{LO}}^{(m)}(t) = E_{\text{LO}} e^{-i(\Omega t + \theta)}$ , where  $E_{\text{LO}}$  is real. The balanced homodyne measurement generates a photocurrent

$$\begin{aligned} I(t) &= \text{Re} \left[ \hat{E}^{(m)} E_{\text{LO}}^{(m)*} \right] \\ &= \text{Re} \left[ E_{\text{LO}} e^{i\theta} (\hat{a}_c^{(m)'} + \hat{a}_+^{(m)'} e^{-i\omega_c t} + \hat{a}_-^{(m)'} e^{i\omega_c t}) \right], \end{aligned} \quad (\text{S4})$$

where we have set the electron charge  $q = 1$  for theoretic-

\* Current address: Department of Electronic and Information Engineering, Shanxi University, Taiyuan, China

† zsz@email.arizona.edu

# Equal contributions

cal convenience.

An electronic mixer supplied by an RF LO at  $\omega_c$  and with a phase  $\phi_0$  is then applied on the photocurrent, i.e.  $\cos(\omega_c t + \phi_0)$ , moving the photocurrent's spectral component at  $\omega_c$  to the baseband. After filtering, the baseband photocurrent reads

$$I_B^{(m)}(t) = -\text{Re} \left[ e^{i\theta} \hat{b}^{(m)\prime} \right], \quad (\text{S5})$$

where we have defined the mode

$$\hat{b}^{(m)\prime} \equiv (e^{i\phi_0} \hat{a}_+^{(m)\prime} + e^{-i\phi_0} \hat{a}_-^{(m)\prime}) / \sqrt{2}. \quad (\text{S6})$$

In doing so, one only needs to consider measurements on the effective mode  $\hat{b}^{(m)\prime}$  in estimating the parameters of the probed RF field. Likewise, a corresponding effective mode before the RF-to-photonic transduction is defined as

$$\hat{b}^{(m)} \equiv (e^{i\phi_0} \hat{a}_+^{(m)} + e^{-i\phi_0} \hat{a}_-^{(m)}) / \sqrt{2}. \quad (\text{S7})$$

Derived from Eq. S2, the transform of the effective mode through the transduction is

$$\hat{b}^{(m)\prime} = J_0(A_m) \hat{b}^{(m)} + i \sqrt{2} J_1(A_m) \cos(\phi_0 + \varphi_m) \hat{a}_c^{(m)} + \text{v.c.}, \quad (\text{S8})$$

where v.c. are the vacuum modes and higher order zero-mean modes. For  $A_m \ll 1$  and  $|\alpha_m| \gg 1$ , the evolution of  $\hat{b}_m$  through the transduction is well described by a first-order approximation, giving a displacement of  $i \sqrt{2} J_1(A_m) \cos(\phi_0 + \varphi_m) \alpha_m$  on  $\hat{b}_m$  on the phase quadrature. Thus, to access the displacement, the LO phase needs to be set to  $\theta = \pi/2$  to observe the phase quadrature of  $\hat{b}^{(m)}$ , i.e.,  $I_B^{(m)}(t) = \text{Im} [\hat{b}^{(m)\prime}]$ , as experimentally verified by the sinusoidal signal in Fig. 2 of the main text. Moreover, because the RF-field information is transferred to the phase quadrature of the effective mode, a quantum enhancement in the measurement sensitivity requires that the effective mode is in a phase squeezed state. This is achieved by setting the OPA to operate in a parametric amplification regime.

To measure a RF-field phase  $\varphi_m \ll 1$ , we set  $\phi_0 = \mp \pi/2$ , then the effective mode, up to the leading order, becomes

$$\hat{b}^{(m)\prime} = J_0(A_m) \hat{b}^{(m)} + g_m i \sqrt{2} J_1(A_m) \varphi_m \hat{a}_c^{(m)} + \text{v.c.}, \quad (\text{S9})$$

where  $g_m = \pm 1$  can be tuned by the sign of  $\phi_0$ . Here if we further expand  $J_1(A_m) \simeq A_m/2 = \pi \frac{\gamma E_m}{2\sqrt{\pi}}$  and replace  $\hat{a}_c^{(m)}$  with its mean  $a_c^{(m)}$ , the second term becomes  $i\pi g_m \sqrt{2} a_c^{(m)} \frac{\gamma E_m}{2\sqrt{\pi}} \varphi_m$ , i.e., a displacement on the phase quadrature. This expression also agrees with Eq. (2) in the main text.

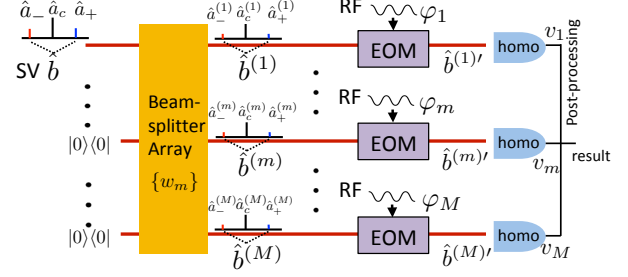


FIG. S1. Theoretical model for the entangled RF-photonic sensor network. SV: squeezed vacuum. EOM: electro-optic modulator. homo: homodyne measurement. At the quantum source, the sideband modes  $\hat{a}_\pm$  are entangled in a two-mode squeezed state, leading to the effective mode  $\hat{b} = i(\hat{a}_+ - \hat{a}_-) / \sqrt{2}$  in a phase SV state. The central spectral mode  $\hat{a}_c$  is close to a coherent state  $|\alpha\rangle$ . A beam splitter array with weights  $\{w_m, 1 \leq m \leq M\}$  generates the CV multipartite entangled state of the effective modes  $\{\hat{b}^{(m)}, 1 \leq m \leq M\}$ . Each  $\hat{b}^{(m)} = i(\hat{a}_+^{(m)} - \hat{a}_-^{(m)}) / \sqrt{2}$  accounts for two sideband modes. The EOM transduces the RF signal into optical field quadrature displacements. Postprocessing of homodyne measurement results at all sensors generates a sum with weights  $\{v_m, 1 \leq m \leq M\}$ , which is used to infer the average RF-field amplitude or the AoA.

## B. Entangled RF-photonic sensor network

Shown in Fig. S1, to apply the DQS protocol developed in Ref. [S1] to an entangled RF-photonic sensor network, the quantum source first effectively generates a single-mode squeezed vacuum mode  $\hat{b} = i(\hat{a}_+ - \hat{a}_-) / \sqrt{2}$ , where  $\hat{a}_\pm$  are the sideband modes. Subsequently, a beam splitter array with weights  $\{w_m, 1 \leq m \leq M\}$  ( $\sum w_m^2 = 1$ ) produces the modes  $\hat{b}^{(m)} = i(\hat{a}_+^{(m)} - \hat{a}_-^{(m)}) / \sqrt{2}$  that are distributed to different sensors. In the experiment, such a state is produced with a two-mode squeezed vacuum state between the sideband modes  $\hat{a}_\pm$  such that  $\langle \hat{a}_+ \hat{a}_- \rangle = \sqrt{N_S(N_S + 1)} e^{i\tau}$  and  $\langle \hat{a}_+^2 \rangle = \langle \hat{a}_-^2 \rangle = 0$ , where  $N_S$  is the mean photon number. The variance of the phase quadrature  $\langle \text{Im} [\hat{b}]^2 \rangle = (2N_S + 1 - 2 \cos \tau \sqrt{N_S(N_S + 1)}) / 4$ . Choosing  $\tau = 0$ , the variance is minimized to

$$\langle \text{Im} [\hat{b}]^2 \rangle = \frac{1}{4 (\sqrt{N_S} + \sqrt{N_S + 1})^2}, \quad (\text{S10})$$

so that a squeezed vacuum state is generated at the effective mode  $\hat{b}$ .

In the beam splitter array, all spectral modes undergo the same transform. Thus, the central spectral modes  $\hat{a}_c^{(m)}$  at different sensors are also generated by splitting the central spectral mode  $\hat{a}_c$  at the source. Prior to the EOM at each sensor,  $\hat{b}^{(m)} = w_m \hat{b} + \text{v.c.}$ ,  $\hat{a}_c^{(m)} = w_m \hat{a}_c + \text{v.c.}$ , and

the effective mode after the EOM becomes

$$\hat{b}^{(m)'} = J_0(A_m)w_m\hat{b} + g_m w_m i \sqrt{2}J_1(A_m)\varphi_m\hat{a}_c + \text{v.c.}, \quad (\text{S11})$$

on which the phase quadrature  $I_B^{(m)}(t) = \text{Im}[\hat{b}^{(m)'}]$  is measured.

Suppose the global parameter to be estimated is  $\bar{\varphi} = \sum_m c_m \varphi_m$ , with weights being  $c_m$  real. To obtain an estimation, a suitable set of  $w_m$ 's is required, and postprocessing on measurement outcomes of all sensors is further needed to construct an unbiased estimator

$$\hat{L} = s \sum_m v_m I_B^{(m)}(t) = s \text{Im} \left[ \sum_m v_m \hat{b}^{(m)'} \right], \quad (\text{S12})$$

where the weights  $v_m$  are real and normalized,  $\sum_m v_m^2 = 1$ , and  $s > 0$  is a scaling factor. The unbiased condition requires the expectation value

$$\langle \hat{L} \rangle = s \sum_m v_m g_m w_m \varphi_m \beta = \sum_m c_m \varphi_m, \quad (\text{S13})$$

where  $\sqrt{2}J_1(A_m)\alpha = \beta$  is fixed. Thus, the chosen  $v_m, w_m$ 's need to make  $c_m = s g_m v_m w_m \beta, \forall m$ .

To use the phase squeezed state in the  $\hat{b}$  mode to minimize the variance of the estimator,  $v_m = w_m$  is needed, and consequently the optimum choices of the parameters are

$$w_m^{\text{opt}} = \frac{\sqrt{|c_m|}}{\sqrt{\sum |c_m|}}, g_m^{\text{opt}} = \text{sign}(c_m), s^{\text{opt}} = \sum |c_m|/\beta. \quad (\text{S14})$$

The minimum variance is thus

$$\text{var}(\hat{L})^{\text{opt}} = \left( \sum |c_m|/\beta \right)^2 \langle \text{Im}[\hat{b}]^2 \rangle, \quad (\text{S15})$$

where the variance of the phase squeezed state is given by Eq. S10.

To show that the weights  $w_m^{\text{opt}}$ 's indeed yield the optimum entanglement-enhanced estimation performance, we choose a set of sub-optimum weights  $\{w_m, 1 \leq m \leq M\}$  and the associated postprocessing weights  $\{v_m, 1 \leq m \leq M\}$  to maintain an unbiased estimator, as specified in Eq. S13. The estimator variance is then derived as following. Denote the effective modes as  $\hat{b}' = (\hat{b}^{(1)'}, \dots, \hat{b}^{(M)'})^T$ , obtained from a beam splitter transform  $\mathbf{T} = (w, \mathbf{T}_1)$  on mode  $\hat{b}$  and vacuum modes  $\hat{e} = (\hat{e}_2, \dots, \hat{e}_M)$ . Here,  $w \equiv (w_1, \dots, w_M)^T$ , i.e.,  $\hat{b}' = (w, \mathbf{T}_1)(\hat{b}, \hat{e})^T$ . From the orthogonality condition,  $\mathbf{T}^T \mathbf{T} = \mathbf{T} \mathbf{T}^T = \mathbf{I}_M$ , one has  $w^T w = 1, w^T \mathbf{T}_1 = 0, \mathbf{T}_1^T \mathbf{T}_1 = \mathbf{I}_{M-1}$ , and  $w w^T + \mathbf{T}_1 \mathbf{T}_1^T = \mathbf{I}_{M-1}$ . Here,  $\mathbf{I}_L$  is an  $L \times L$  identity matrix. Let  $v = (v_1, \dots, v_M)^T$ , the estimator is then written as  $\hat{L} = s \text{Im} [v^T \mathbf{T}(\hat{b}, \hat{e})^T]$ . Thus,

the variance of the estimator

$$\begin{aligned} \text{var}(\hat{L}) &= s^2 v^T \mathbf{T} \text{Diag} \left[ \langle \text{Im}[\hat{b}]^2 \rangle, \frac{1}{4} \mathbf{I}_{M-1} \right] \mathbf{T}^T v \\ &= s^2 (v^T w)^2 \langle \text{Im}[\hat{b}]^2 \rangle + \frac{1}{4} s^2 v^T \mathbf{T}_1 \mathbf{T}_1^T v \\ &= s^2 (v^T w)^2 \left( \langle \text{Im}[\hat{b}]^2 \rangle - \frac{1}{4} \right) + \frac{1}{4} s^2 v^T v \\ &= \frac{1}{\beta^2} \left[ \left( \sum_{m=1}^M g_m c_m \right)^2 \left( \langle \text{Im}[\hat{b}]^2 \rangle - \frac{1}{4} \right) + \frac{1}{4} \left( \sum_{m=1}^M \frac{c_m^2}{w_m^2} \right) \right], \end{aligned} \quad (\text{S16})$$

where  $v^T w = \sum_{m=1}^M g_m c_m / s \beta$  and  $v^T v = \sum_{m=1}^M c_m^2 / (s^2 w_m^2 \beta^2)$  have been used. Again, the variance of the phase squeezed state is given in Eq. S10. To rederive the optimum parameters  $w_m$ 's and  $g_m$ 's, the constraint  $\sum_{m=1}^M w_m^2 = 1$  is considered. Using Lagrangian multipliers, it becomes easy to see that  $w_m \propto \sqrt{|c_m|}$ . Also, since  $\langle \text{Im}[\hat{b}]^2 \rangle - \frac{1}{4} \leq 0$  due to squeezing,  $g_m = \text{sign}(c_m)$  is needed. The same solution as in Eq. S14 for the optimum parameters is then derived.

The above analysis applies to an ideal lossless situation. In a practical scenario, however, loss  $1 - \eta$  is present at each sensor. Effectively, loss can be accounted for at the source by replacing Eq. S10 with

$$\langle \text{Im}[\hat{b}]^2 \rangle = \frac{1}{4} \left[ \frac{\eta}{(\sqrt{N_S} + \sqrt{N_S + 1})^2} + (1 - \eta) \right], \quad (\text{S17})$$

where  $\eta$  is the transmissivity. The optimum solutions in Eq. S14 and Eq. S15, as well as the variance in Eq. S16 remains valid with  $\beta = \sqrt{\eta} \sqrt{2} J_1(A_m) \alpha$ .

### C. Performance analysis

To compare the performance of quantum sensing protocols, one should first identify the resource constraints. Various theoretical works simply consider an energy constraint, i.e., by fixing the total mean photon numbers employed in different protocols under comparison. The energy constraint is valid in scenarios where the interrogated sample is sensitive to the probe power caused by, e.g., photodamage or self-concealing. In RF-photonics sensing and LIGO, however, the optical power should ideally be cranked up as much as one can until the device power accommodation limit is arrived. Therefore, in an RF-photonics sensor, the power carried by the central mode  $\hat{a}_c$  needs to be large, subject to the operational limit of the device. For example, integrated RF-photonics sen-

sors can accommodate milliwatts of optical power [S2]. In a classical separable RF-photonic sensor network, the effective mode  $\hat{b}$  is in a vacuum state, and the laser power distribution to different sensors is optimized through tuning the beam-splitter ratios.

In an entangled RF-photonic sensor network, phase squeezed light resides in the effective mode  $\hat{b}$ . Because the experimental energy the squeezed state  $N_S \ll |\alpha|^2$ , it is negligible, as compared to that of the central spectral mode. As such, the performance comparison between the classical separable and entangled sensor networks is based on setting the classical scheme's  $\hat{b}$  in a vacuum state and the entangled scheme's  $\hat{b}$  to a squeezed state while employing identical energies on the central spectral modes for both cases. The estimation variances for both schemes are modeled by Eq. S15, with  $\langle \text{Im}[\hat{b}]^2 \rangle$  given in Eq. S17 for the entangled sensor network and  $\langle \text{Im}[\hat{b}]^2 \rangle = 1/4$  for the classical separable sensor network.

To show that the quantum state shared by the sensors is indeed entangled, we performed a theoretical comparison between the DQS scheme and the optimum separable scheme, subject to a total photon number constraint in the  $\hat{b}_m$  modes for both cases. As analyzed in Ref. [S1, S3], in the absence of loss, the optimum separable DQS utilizes  $\{\hat{b}^{(m)}, 1 \leq m \leq M\}$  modes in a product of squeezed vacuums, with the optimum mean photon number distribution  $N_S^{(m)}$  under the constraint  $\sum_{m=1}^M N_S^{(m)} = N_S$ . Suppose the same beam splitter array is used to distribute the central spectral mode's coherent state to different sensors, the unbiased estimator condition remains the same as Eq. S13. Now, the  $\hat{b}^{(m) \prime}$  modes are separable, each having a variance of

$$\text{var}(\text{Im}[\hat{b}^{(m) \prime}]) = \frac{1}{4} \left[ \frac{\eta}{(\sqrt{N_S^{(m)}} + \sqrt{N_S^{(m)}} + 1)^2} + (1 - \eta) \right]. \quad (\text{S18})$$

Akin to Eq. S16, the estimation variance

$$\text{var}(\hat{L}) = \sum_{m=1}^M \frac{c_m^2}{w_m^2 \beta^2} \text{var}(\text{Im}[\hat{b}^{(m) \prime}]). \quad (\text{S19})$$

For a set of fixed  $w_m$ 's, one optimizes  $N_S^{(m)}$  to minimize the estimation variance. One can show the overall minimum is achieved at  $w_m^2 \propto c_m \sqrt{\text{var}(\text{Im}[\hat{b}^{(m) \prime}])}$ :

$$\text{var}(\hat{L})^* = \min_{\sum_m N_S^{(m)} = N_S} \sum_{m=1}^M \frac{c_m}{\beta} \sqrt{\text{var}(\text{Im}[\hat{b}^{(m) \prime}])}. \quad (\text{S20})$$

In our experiment, at the source we measured the anti-

squeezing level as  $\sim 10$  dB above the shot-noise level and the squeezing level as  $\sim 4$  dB below the shot-noise level, from which we can infer the ideal source squeezing as  $\sim 11.7$  dB and mean photon number  $N_S \sim 3.3$ . In the field amplitude measurement, the measured squeezing was  $\sim 3.2$  dB (noise variance  $\sim 0.48$  of that of the shot noise) for the three sensor network case. Thus, the overall efficiency  $\eta \sim 0.56$  are then derived. With equal weights, the optimum separable scheme employs  $\sim 7.9$  dB of squeezing at the local source, to match the total mean photon number in squeezing, and achieves a 2.7 dB of noise reduction (noise variance  $\sim 0.53$  of the shot noise). This leads to a  $\sim 10\%$  advantage in estimation variance for our experimental result over that of the optimum separable sensor network, thereby verifying the entanglement shared by the sensors.

It is worth noting that the optimum separable RF-photonic sensor network discussed above requires that each sensor has its own squeezed-light source, which induces a substantial resource overhead.

#### D. Finite difference method for the estimation of AoA of the RF field

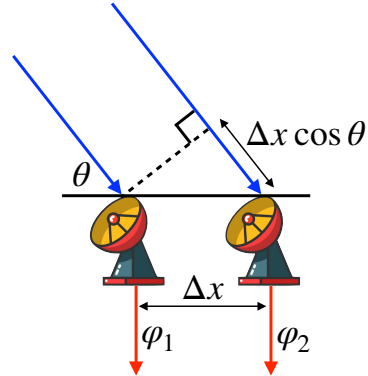


FIG. S2. A simple scheme to estimate the AoA of an incident RF field based on phase difference ( $\varphi_2 - \varphi_1$ ) measurement at two RF sensors. Dashed line is the wavefront of the RF field.

A simple example of measuring the AoA of an incident RF field is illustrated in Fig. S2. The AoA  $\theta$  is related to the relative phase of the two sensors by

$$\frac{\varphi_2 - \varphi_1}{2\pi} = \frac{\Delta x \cos \theta}{\lambda} + k, \quad (\text{S21})$$

where  $\lambda$  is the wavelength of the RF field, and  $k$  is an integer.  $k$  can be set to 0, if the sensors are located close to a less than a wavelength, i.e.,  $\Delta x/\lambda \ll 1$ , but the measurement of the AoA, in general, is not restricted to this

assumption. The AoA can then be estimated as

$$\theta = \arccos \frac{(\varphi_2 - \varphi_1)\lambda}{2\pi\Delta x}. \quad (\text{S22})$$

Since both  $\lambda$  and  $\Delta x$  are predetermined, the measurement of the AoA of an RF field is transformed into a difference phase estimation problem undertaken by the two sensors, which is a focus of the present article. Now we characterize the discretization error and optimize the precision of phase-difference estimation.

We will consider the three-point case,  $x_1 < x_2 < x_3$ , suppose the weights are  $c_1, c_2, c_3$ . The estimator is

$$\hat{L} = c_1\varphi(x_1) + c_2\varphi(x_2) + c_3\varphi(x_3). \quad (\text{S23})$$

*Case 1.*— Phase-difference estimation at a central node.

$$\begin{aligned} \varphi(x_1) &= \varphi(x_2) - \varphi^{(1)}(x_2)\Delta x + \frac{1}{2}\varphi^{(2)}(x_2)\Delta x^2 + O(\Delta x^3), \\ \varphi(x_3) &= \varphi(x_2) + \varphi^{(1)}(x_2)\Delta x + \frac{1}{2}\varphi^{(2)}(x_2)\Delta x^2 + O(\Delta x^3). \end{aligned} \quad (\text{S24})$$

One requires  $c_3 = 1 + c_1, c_2 = -1 - 2c_1$  to ensure the expectation value  $\langle \hat{L} \rangle = \varphi^{(1)}(x_2)\Delta x + O(\Delta x^2)$ . In particular if we require  $c_1 + c_3 = 0$ , or  $(c_1, c_2, c_3) = (-1/2, 0, 1/2)$ , then  $\langle \hat{L} \rangle = \varphi^{(1)}(x_2)\Delta x + O(\Delta x^3)$ .

With the proper chosen weights in Eq. S14, the variance in Eq. S15 is

$$\text{var}(\hat{L}) = \left( \sum |c_m|/\beta \right)^2 \langle \text{Re}\hat{b}^2 \rangle \propto (|c_1| + |1 + 2c_1| + |1 + c_1|)^2. \quad (\text{S25})$$

It is minimized when  $c_1 = -1/2$ . Thus, it is always optimum to use  $(c_1, c_2, c_3) = (-1/2, 0, 1/2)$ , because this minimizes both the estimation variance and the discretization error for the phase gradient.

*Case 2.*— Phase-difference estimation at an edge node.

$$\begin{aligned} \varphi(x_2) &= \varphi(x_1) + \varphi^{(1)}(x_1)\Delta x + \frac{1}{2}\varphi^{(2)}(x_1)\Delta x^2 + O(\Delta x^3), \\ \varphi(x_3) &= \varphi(x_1) + \varphi^{(1)}(x_1)2\Delta x + \frac{1}{2}\varphi^{(2)}(x_1)4\Delta x^2 + O(\Delta x^3). \end{aligned} \quad (\text{S26})$$

One requires  $c_2 = 1 - 2c_3, c_1 = c_3 - 1$  to ensure the expectation value  $\langle \hat{L} \rangle = \varphi^{(1)}(x_1)\Delta x + O(\Delta x^2)$ . If  $c_2 + 4c_3 = 0$  is required, then  $(c_1, c_2, c_3) = (-3/2, 2, -1/2)$  and  $\langle \hat{L} \rangle = \varphi^{(1)}(x_1)\Delta x + O(\Delta x^3)$ .

A similar analysis can be performed for the second-order derivative, except that there is only one possible set of parameters for each case. To estimate at a central node, one needs  $c_1 = c_3 = 1/2, c_2 = -1$ , so  $\langle \hat{L} \rangle = \varphi^{(2)}(x_2)\Delta x^2 + O(\Delta x^4)$ . To estimate at an edge

node, one needs  $c_1 = 1, c_2 = -2, c_3 = 1$ , so  $\langle \hat{L} \rangle = \varphi^{(2)}(x_1)\Delta x^2 + O(\Delta x^3)$ .

## II. EXPERIMENTAL DETAILS

Here, we provide more details about the experimental setup and the acquired data. Sec. II A introduces the components used in the experiment and the phase-locking mechanisms. Sec. II A provides data of the calibration of the shot-noise level, the electronic noise floor, and the squeezing level at different RF frequencies. Sec. II C elaborates the performance of each individual sensor at different input power levels and shows a nice agreement between the experimental data and a theoretical model.

### A. Detailed description of experimental setup

A detailed experimental diagram is drawn in Fig. S3. A 1550-nm mode-hop-free semiconductor laser (New Focus Velocity TLB-6728) generates  $\sim 10$  mW of light, which is modulated by a fiber-based phase modulator (PM) driven by a 24-MHz signal to create two sidebands for cavity locking based on the Pound-Drever-Hall (PDH) technique. The modulated light is subsequently boosted to  $\sim 1$  W by an erbium-doped fiber amplifier (EDFA) and coupled to free space. The 1550-nm light is first filtered by a locked 1550-nm mode-cleaning cavity (MC) and then split into two arms to serve, respectively, as the pump for second-harmonic generation (SHG) and the LO for homodyne measurements. The semi-monolithic SHG cavity entails a curved cavity mirror with 10% reflectivity at 775 nm and 94% reflectivity at 1550 nm [S4] and a type-0 periodically-poled KTiOPO<sub>4</sub> (PPKTP) crystal temperature stabilized at 34.0°C. The PPKTP crystal has a curved facet being highly reflective at 1550 nm and 775 nm and a flat facet that is anti-reflection coated at both wavelengths. The SHG cavity is locked using the 24-MHz sideband and generates  $\sim 300$  mW of 775-nm light under a 500-mW 1550-nm pump. The 775-nm light is first filtered by a locked 775-nm MC and then injected through a curved cavity mirror into an OPA cavity where a second identical PPKTP crystal temperature stabilized at 40.5°C is embedded. The curved mirror of the OPA cavity has 95% reflectivity at 775 nm and 87.5% reflectivity at 1550 nm. To generate phase squeezed light, a weak 1550-nm beam is tapped from the LO and modulated by a free-space PM to create 20-MHz sidebands. The modulated weak 1550-nm beam is reflected on a 775-nm/1550-nm dichroic beam splitter (DBS) and then

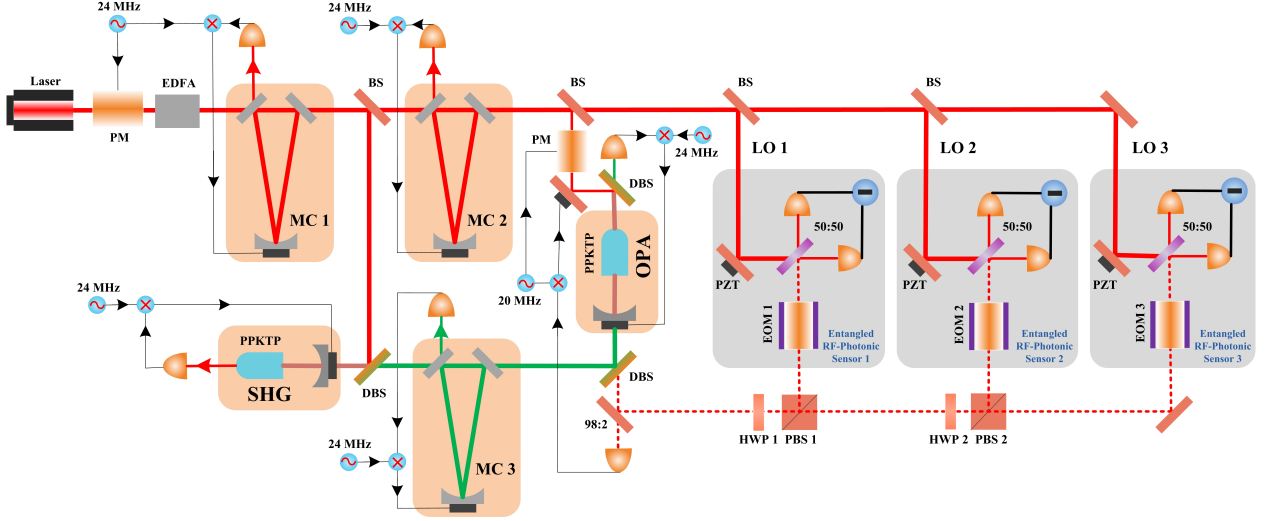


FIG. S3. Detailed experimental diagram. EOM: electro-optic modulator; MC: mode-cleaning cavity; BS: beam splitter; LO: local oscillator; DBS: Dichroic beam splitter; PPKTP: periodically-poled  $\text{KTiOPO}_4$ ; OPA: optical parametric amplifier; SHG: second-harmonic generation; PBS: polarizing beam splitter; PM: phase modulator; HWP: half-wave plate; PZT: piezoelectric transducer.

seeds the OPA cavity. The OPA cavity is locked by the 24-MHz sideband of the 775-nm light that transmits through the DBS. 2% of the 1550-nm output from the OPA curved cavity mirror is tapped and is employed to lock the phase between the 1550-nm seed beam and the 775-nm pump using the 20-MHz sidebands so that the OPA operates in a parametric amplification regime. When phase locked, the OPA cavity emits quantum light composed of an effective squeezed vacuum state residing in the 11-MHz sideband modes while the central spectral mode is a displaced phase squeezed state. Due to the large quadrature displacement, the central spectral mode can be well approximated by a classical coherent state. The single spatial-mode quantum light is diverted into three RF-photonic sensors by two variable beam splitters (VBSs), each consisting of a half-wave plate (HWP) and a polarizing beam splitter (PBS). The splitting ratios of both VBSs determines the CV multipartite entangled state. Each RF-photonic sensor is equipped with an EOM driven by the probed RF signal with 11-MHz carrier frequency. Due to the phase modulation, a portion of the coherent state in the central mode is transferred to quadrature displacement at the 11-MHz sidebands that accommodate the phase squeezed state. The magnitude of the quadrature displacement is dependent on the amplitude and phase of the probed RF field, as described by Eq. 1 of the main text and analyzed in Supplemental Information I. After the EOM, the quantum signal and the LO interfere on a 50:50 BS. By fine tuning the spot sizes of both beams, a classical interference

visibility in excess of 97% was achieved at each sensor. The two outputs of the BS are detected by two photodiodes, each with  $\sim 88\%$  quantum efficiency, in a balanced homodyne configuration. The difference photocurrent is amplified by a transimpedance amplifier with a gain of  $20 \times 10^3$  V/A. The DC component of the output voltage signal is utilized to lock the phase between the LO and the quantum signal so that the LO always addresses the squeezed phase quadrature with the displacement. The 11-MHz component of the voltage signal from each sensor is first demodulated by an electronic mixer, filtered by a 240-kHz low-pass filter, and recorded by an oscilloscope (LeCroy WaveRunner 8404 M) with a 4-GHz analog bandwidth (only 200 MHz bandwidth was used) at a 50 M Samples/s/channel sampling rate. Postprocessing derives the estimation and measurement noise variances.

## B. Calibration of shot-noise and squeezing levels

Prior to taking data, we first calibrated the shot-noise level and compared it with the electronic noise floor. To do so, a local oscillator with 14.1 mW power was fed to the homodyne detector of Sensor 1 while the signal input to the detector was blocked. Setting the resolution bandwidth of the RF spectrum analyzer to 300 kHz and the video bandwidth to 300 Hz, the noise power spectrum of the homodyne detector is found flat beyond 1.9 MHz, showing shot-noise limited behavior (red curve of Fig. S4). The measured shot-noise level agreed pre-

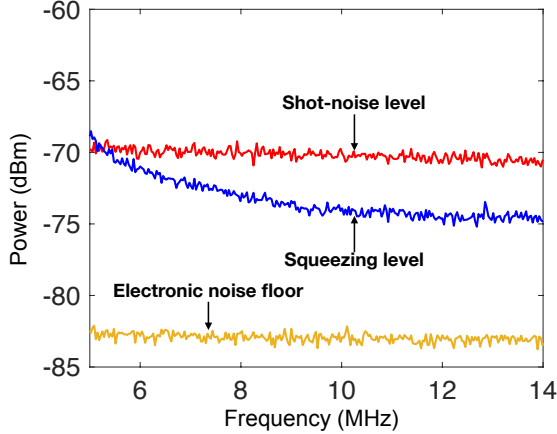


FIG. S4. Calibration of the shot-noise and squeezing levels. The shot-noise (squeezing) level is represented by the red (blue) curve, while the electronic noise floor is plotted in the yellow curve as a comparison. All measurements were taken with a resolution bandwidth of 300 kHz and a video bandwidth of 300 Hz.

cisely with a model that accounted for the local oscillator power, detector quantum efficiency, the gains of the amplifiers, and the resolution bandwidth of the RF spectrum analyzer. As a comparison, the electronic noise floor of the homodyne detector was measured by blocking the local oscillator and is depicted in the yellow curve in Fig. S4. The shot-noise level is 13 dB higher than the electronic noise floor, allowing for the observation of sub-shot-noise behavior enabled by squeezed light.

We then measured the squeezing level at different RF frequencies. In the measurement, the OPA was locked to operate in the parametric amplification regime to produce phase squeezed light, and the relative phase between the squeezed light and the local oscillator was locked to  $\pi/2$  so that the local oscillator was ensured to address the phase quadrature of the squeezed light. The measured squeezing level is plotted in the blue curve of Fig. S4. Sub-shot-noise behavior was observed at frequencies higher than  $\sim 5.5$  MHz. Squeezing was not observed at lower frequencies, likely due to the residue amplified spontaneous emission noise and the Brillouin scattering noise after the mode-cleaning cavities. Using mode-cleaning cavities with narrower linewidths, one may observe squeezing at lower frequencies. At 11 MHz, the carrier frequency of the probed RF field, the observed squeezing level was  $\sim 4$  dB, consistent with other experimental data.

### C. Performance of individual sensors

In the entangled sensor network, the three RF-photon sensors receive different portions of the original squeezed light, based on the splitting ratios of the VBSs determined by a specific distributed sensing task. To quantify the performance of each sensor at a certain input power level, the amount of noise power arising from the homodyne measurements is recorded under different input power levels. We first fix the splitting ratio of VBS 2 at 50:50 while varying the splitting ratio of VBS 1 from 0:100 to 100:0. In doing so, Sensor 1's received portion of the squeezed light varies from 0% to 100%, while Sensor 2 and Sensor 3 equally share the rest of the power. The resulting noise powers for the three sensors at different splitting ratios of VBS 1 are plotted in Fig. S5a. We then fix the splitting ratio of VBS 2 at 0:100 while varying the splitting ratio of VBS 1 from 100:0 to 0:100. In doing so, the squeezed light is split between Sensor 1 and Sensor 3 with different ratios, while Sensor 2 is unused. The corresponding noise powers for Sensor 1 and Sensor 2 are recorded and plotted in Fig. S5b. Finally, the splitting ratio of VBS 1 is fixed at 50:50, and that of VBS 2 is varied from 100:0 to 0:100. In this set of measurements, Sensor 1 always receives 50% of the squeezed light, while Sensor 2 and Sensor 3 share the rest 50% with various ratios. The noise powers for all three sensors at different splitting ratios are recorded and plotted in Fig. S5c. In all three sets of measurements, the experimental data are compared with a theoretical model, as depicted in the solid curves. Nice agreement between the theory and experimental data is found.

### D. Additional experimental data

#### 1. Phase-difference estimation at a central node

In addition to the data reported in the main text, we experimentally estimated the phase difference at a central node, served by Sensor 2. To do so, the weights for the optimum CV multipartite entangled state is  $[1/2, 0, -1/2]$ , generated by setting the splitting ratios of VBS 1 and 2 to 50:50 and 0:100. The AoA is emulated by an RF-field phase difference across the three sensors. The negative sign in the weights is introduced by adding a  $\pi$ -phase delay at Sensor 3. In the measurement, the RF phase at Sensor 1 is swept from 0.17 rad to -0.17 rad, and at the same time the RF phase at Sensor 2 is swept from -0.17 rad to 0.17 rad, while the RF-field amplitudes are set identical. The homodyne data from the three sensors are weighted to obtain an unbiased estimator. The estimated phase difference vs. the applied RF-field phase are plot-

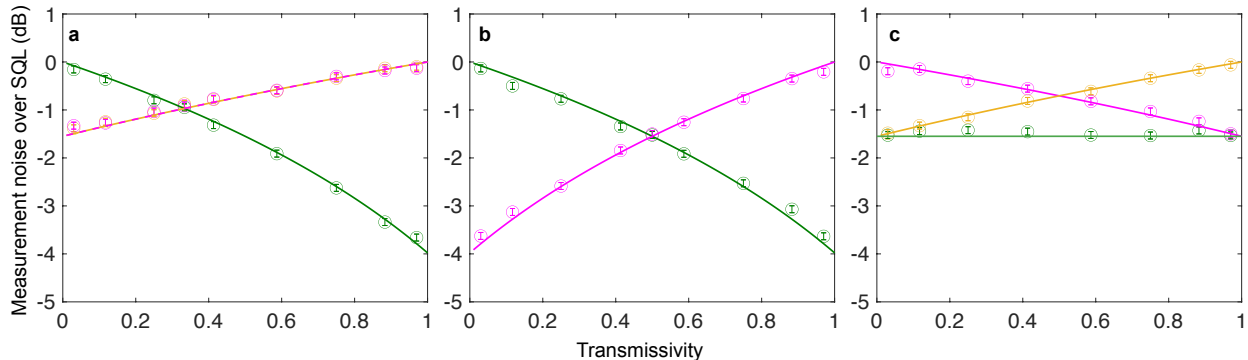


FIG. S5. The measurement noise powers at the three sensors under different input power levels, tuned by a VBS. (a) The splitting ratio of VBS 2 was fixed at 50:50 while that of VBS 1 was varied from 0:100 to 100:0. (b) The splitting ratio for VBS 2 was fixed at 0:100 while that of VBS 1 was varied from 100:0 to 0:100. (c) The splitting ratio of VBS 1 was fixed at 50:50 while that of VBS 2 was varied from 100:0 to 0:100. Experimental data are plotted in green circles for Sensor 1, gold circles for Sensor 2, and magenta circles for Sensor 3. Solid curves represent theoretical predictions. Error bars account for estimated uncertainties arising from experimental instabilities.

ted as blue circles in Fig. S6a and compared to the classical separable scheme (red triangles), with the shaded area representing the estimation uncertainties, showing a 3.5-dB reduction for the entangled case. Figure S6b plots the measurement noise and estimation variances at the two sensors in performing the phase-difference estimation at a central node.

## 2. Optimization of multipartite entangled state

In addition to optimizing the CV multipartite entangled state for estimating phase difference at an edge node, we also measured the estimation variances under different quantum circuit settings for the task of estimating the average RF-field amplitude and the task of estimating the phase difference at a central node. Fig. S7a plots the comparison on the estimation variances between the classical separable and entangled sensor networks. To optimize the CV multipartite entangled state, the splitting ratio for VBS 2 is fixed at 50:50 while the splitting ratio for VBS 1 is tuned from 100:0 to 0:100. The largest advantage for the entangled sensor network occurs at a transmissivity of 0.33 for VBS 1, when all sensors receive equal amount of optical power. The experimental data agree very well with the theoretical predictions represented by the solid lines (See Sec. IIE for more details). In optimizing the CV multipartite entangled state for phase-difference estimation at a central node, the splitting ratio for VBS 2 is kept 0:100 while the splitting ratio for VBS 1 is tuned between 100:0 to 0:100. The negative sign in transmissivity represents a

sign flip on the homodyne data in postprocessing, as articulated in the main text. Fig. S7b plots a comparison on the estimation variances between the classical separable and entangled sensor networks in the task of phase-difference estimation at a central node. As discussed in the main text, the asymmetric behavior is a signature for the quantum correlations between the measurement noise at different sensors. The experimental data show nice agreement with our theoretical model.

## E. Theoretical model for the experiment

In the entangled RF-photon sensor network, let the global parameter to be estimated be a weighted average of the phase of the RF field at different sensors, i.e.,  $\bar{\varphi} = \sum_m c_m \varphi_m$ , with the weights  $c_m$ 's being real. Also the estimation of any analytical function of  $\varphi_m$ 's can be reduced to the estimation of weighted sum by linearization and adopting adaptivity [S5]. The average field-amplitude estimation problem can be formulated in a similar way. Under beam splitter ratios  $\{w_m\}$  for amplitude and  $\{g_m = \pm 1\}$  determined by RF phase delays at the sensors, the estimation variance can be derived as

$$\text{var} = \frac{1}{\beta^2} \left[ \left( \sum_{m=1}^M g_m c_m \right)^2 \delta_b + \frac{1}{4} \left( \sum_{m=1}^M \frac{c_m^2}{w_m^2} \right) \right].$$

Here,  $\beta$  is a coefficient determined by the mean photon number of the baseband light, the transduction efficiency of the EOM, and the system efficiency.  $\delta_b \equiv \eta \langle \text{Im} [\hat{b}]^2 \rangle - \eta/4$ , with  $\langle \text{Im} [\hat{b}]^2 \rangle$  being the variance of the

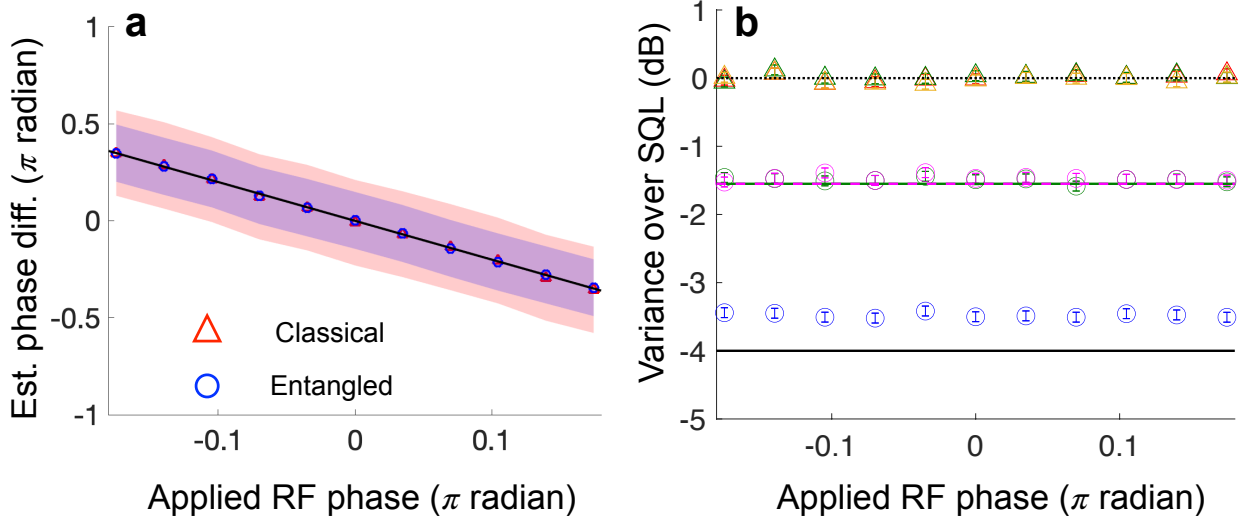


FIG. S6. (a) Estimation of phase difference at a central node. Circles: data for entangled sensors; triangles: data for classical separable sensors. Shaded area: estimation uncertainties for the entangled (blue) and classical separable (red) sensor networks. The entangled sensor network show a clear reduced estimation uncertainty. (b) Noise variance vs. phase difference at a central node. Measurement noise variances are plotted in green for Sensor 1 and magenta for Sensor 3. Estimation variances, normalized to the SQL, for entangled (blue) and classical separable (red) sensor networks. Green and gold solid horizontal lines: theory curves for noise variances at two sensors. Solid black horizontal line: ideal estimation variance for entangled sensors; experimental deviation likely caused by imperfect phase locking between sensors. Dotted black horizontal line: the SQL for measurement noise variances and normalized estimation variances. While all classical data stay at the SQL, the estimation variances for the entangled sensor networks are sub-SQL and are significantly lower than the measurement noise variances at single sensors. Error bars reflect estimated measurement uncertainties caused by system instabilities.

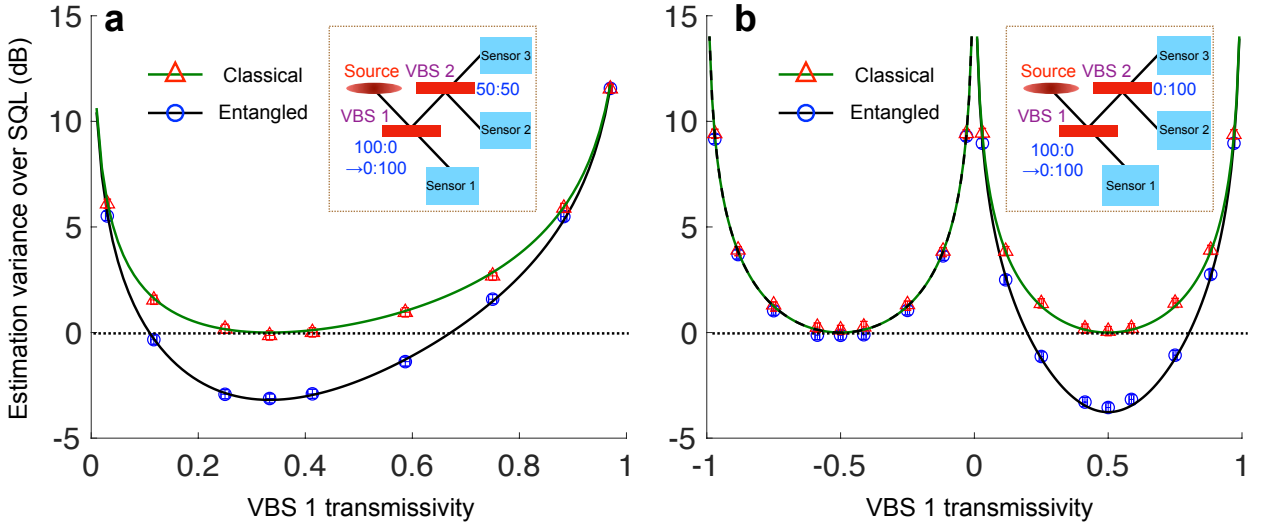


FIG. S7. Optimization of CV multipartite entangled state for the tasks of (a) estimating the average RF-field amplitude and (b) estimating the phase difference at a central node. Circles: entangled sensors data; triangles: classical separable sensors data; black curves: quantum theory; green curves: classical theory. Black horizontal dotted line: the SQL. Error bars account for estimated uncertainties arising from experimental instabilities. The symmetric classical curves vs. the asymmetric quantum curves in (b) manifests the correlated quantum noise arising from the homodyne detectors at different sensors. Insets: illustration of the tuning ranges of the VBS splitting ratios.

phase squeezed state at the source (shot-noise variance is  $1/4$ ) and  $1 - \eta$  being the overall loss seen by each sen-

sor.  $\delta_b = 0$  in the classical separable case and  $\delta_b < 0$  in the entangled case. The optimum parameter choices are thus  $w_m^{\text{opt}} = \sqrt{|c_m|} / \sqrt{\sum |c_m|}$  and  $g_m^{\text{opt}} = \text{sign}(c_m)$ , leading to a minimum estimation variance  $(\sum |c_m|)^2 \langle \text{Im}[\hat{b}]^2 \rangle / \beta^2$  (See Sec. I for derivation details).

The above result is used to model the experimental data in Fig. S7 and Fig. 5 of the main text. To facilitate the comparison, the minimum estimation variance of a classical separable sensor network,  $(\sum |c_m|)^2 / (4\beta^2)$ , is set as the SQL. In Fig. S6c, d, Fig. S7, and Figs. 4, 5 of the main text, the estimation variances are normalized to the SQL unit. The estimation of the average RF-field amplitude requires  $c_1 = c_2 = c_3 = 1/3$  and  $g_1 = g_2 = g_3 = 1$ . In the experiment, the splitting ratio of VBS 1,  $r$ , is tuned from 0:100 to 100:0 while the splitting ratio of VBS 2 is kept 50:50, so that  $w_1 = \sqrt{r}$ ,  $w_2 = w_3 = \sqrt{(1-r)/2}$ . This leads to  $\text{var} = (1/\beta^2)(\delta_b + [1/(1-r) + 1/4r] / 9)$ , with the minimum achieved at  $r = 1/3$ . The theory and the experimental data are plotted in Fig. S7a, showing excellent agreement. To estimate the phase difference at a central node, we set  $c_1 = 1/2$ ,  $c_2 = 0$ ,  $c_3 = -1/2$ . The splitting ratio of VBS 1,  $r$ , is tuned between 100:0 and 0:100 while the splitting ratio of VBS 2 is kept 0:100, corresponding to  $w_1 = \sqrt{|r|}$ ,  $w_2 = 0$ ,  $w_3 = \sqrt{1-|r|}$  and  $g_1 = \text{sign}(r)$ ,  $g_2 = 1$ ,  $g_3 = -1$ . Here,  $g_m = -1$  indicates a  $\pi$ -phase shift on the RF field probed by the  $m$ -th sensor, which can be effectively viewed as applying a  $\pi$ -phase shift on its received entangled state while ensuring an unbiased estimator. For  $r > 0$ ,  $\text{var}_+ = (1/\beta^2)(\delta_b + [1/(1-r) + 1/r] / 16)$ , which is minimized at  $r = 1/2$ , as seen in the right half of Fig. S7(b). We then set  $r < 0$ , leading to  $\text{var}_- = (1/\beta^2)[1/(1-|r|) + 1/|r|] / 16$ . Since  $\delta_b$  is absent in  $\text{var}_-$ , the estimation variances for the entangled and classical separable cases are identical and are both minimized at  $r = -1/2$ , as shown in the left half of Fig. S7(b). The estimation of the phase difference at an edge node requires  $c_1 = 2$ ,  $c_2 = -3/2$ ,  $c_3 = -1/2$ . The splitting ratio of VBS 1 is kept 50:50 while the splitting ratio for VBS 2,  $r$ , is tuned between 100:0 and 0:100, corresponding to  $w_1 = \sqrt{1/2}$ ,  $w_2 = \sqrt{(1-|r|)/2}$ ,  $w_3 = \sqrt{|r|/2}$  and  $g_1 = 1$ ,  $g_2 = -1$ ,  $g_3 = -\text{sign}(r)$ . We first set  $r > 0$ , leading to  $\text{var}_+ = (1/\beta^2)(16\delta_b + [8 + 9/2(1-r) + 1/2r] / 4)$ , which is plotted with the experimental data in the right half of Fig. 5 of the main text. The minimum estimation vari-

ance is achieved at  $r = 1/4$ . We then set  $r < 0$ , leading to  $\text{var}_- = (1/\beta^2)(9\delta_b + [8 + 9/2(1-|r|) + 1/2|r|] / 4) > \text{var}_+$ , as plotted with the experimental data in the left half of Fig. 5 of the main text. The minimum estimation variance is achieved at  $r = -1/4$ .

### III. ENTANGLEMENT DISTRIBUTION

We have demonstrated an entangled sensor network in a free-space table-top experimental platform. For sensors spatially separated over a distance, low-loss optical fibers can be used to distributed the CV multipartite entanglement. State-of-the-art low-loss optical fibers have achieved 0.14 dB/km loss [S6], which will allow the entangled sensor network to achieve an appreciable quantum advantage over classical separable sensor networks over a few tens of kilometers. To show the feasibility of entanglement distribution, we simulated the performance of the entangled sensor network connected by low-loss optical fibers using the experimental parameters for the squeezing level, detector efficiency, and additional loss. The result is depicted in Fig. S8, showing a 2-dB (1-dB) estimation variance reduction for sensors 10 km (30 km) apart from the entanglement source. One interesting fact is that the entanglement-enhanced measurement sensitivity degrades at longer distances but never diminishes.

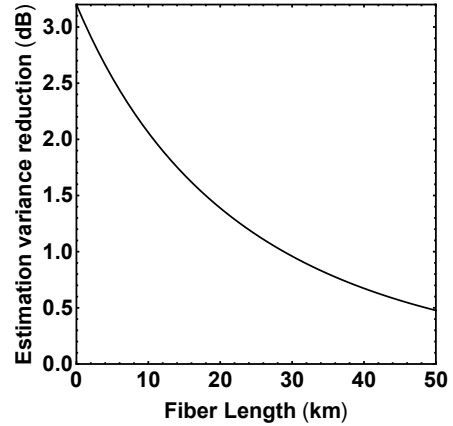


FIG. S8. Simulated estimation variance reduction in an entangled sensor network in which sensors are connected by low-loss optical fibers (0.14 dB/km).

- 
- [1] Q. Zhuang, Z. Zhang, and J. H. Shapiro, Distributed quantum sensing using continuous-variable multipartite entanglement, *Phys. Rev. A* **97**, 032329 (2018).  
[2] W. Jiang *et al.*, Efficient bidirectional piezomechanical transduction between microwave and

- optical frequency, arXiv:1909.04627.  
[3] Y. Xia, Q. Zhuang, W. Clark, and Z. Zhang, Repeater-enhanced distributed quantum sensing based on continuous-variable multipartite entanglement, *Phys. Rev. A* **99**, 012328 (2019).

- [4] M. Mehmet, S. Ast, T. Eberle, S. Steinlechner, H. Vahlbruch, and R. Schnabel, Squeezed light at 1550 nm with a quantum noise reduction of 12.3 dB, *Opt. Express* **19**, 25763 (2011).
- [5] K. Qian, Z. Eldredge, W. Ge, G. Pagano, C. Monroe, J. V. Porto, and A. V. Gorshkov, Heisenberg-scaling measurement protocol for analytic functions with quantum sensor networks, *Phys. Rev. A* **100**, 042304 (2019).
- [6] Y. Tamura, H. Sakuma, K. Morita, M. Suzuki, Y. Yamamoto, K. Shimada, Y. Honma, K. Sohma, T. Fujii, and T. Hasegawa, The First 0.14-dB/km Loss Optical Fiber and its Impact on Submarine Transmission, *J. Light. Technol.* **36**, 44–49 (2018).